Applied Physics Letters ARTICLE pubs.aip.org/aip/apl

In situ growth of carbon nanotubes in biomass carbon for energy storage: The denser the better?

Cite as: Appl. Phys. Lett. **126**, 233904 (2025); doi: 10.1063/5.0268260
Submitted: 28 February 2025 · Accepted: 29 May 2025 ·
Published Online: 10 June 2025

Manish Neupane,[1] Xiahua Zhong,[1] Guanhui Gao,[2] Qiangu Yan,[3] Jinwu Wang,[3] Zhiyong Cai,[3,a)] and Yingchao Yang[1,a)]

AFFILIATIONS

[1]Department of Mechanical and Aerospace Engineering, University of Missouri, 416 S. 6th St., Columbia, Missouri 65211, USA
[2]Electron Microscopy Core, University of Houston, 4218 M.L. King Blvd., Houston, Texas 77204, USA
[3]Forest Product Laboratory, USDA, 1 Gifford Pinchot Dr., Madison, Wisconsin 53726, USA

[a)]**Authors to whom correspondence should be addressed:** zhiyong.cai@usda.gov and yingchao.yang@missouri.edu

ABSTRACT

Carbon nanotubes (CNTs) and their allotropes have been regarded as promising materials for electric double-layer supercapacitors (EDLCs). It is well accepted that the higher surface area of carbon will enable a higher capacity of energy storage. An interesting question is what could happen if the half channel size is less than the Stern layer spacing. In this study, we grew CNTs into carbonized basswood for EDLCs, in which the CNT density varied in bass carbon sheets with different thicknesses, eventually giving various pore/channel sizes. Electrochemical analyses revealed that the bass carbon with a higher CNT density exhibits inferior performance compared to specimens with lower CNT densities. Further investigation through electrochemical impedance spectroscopy suggests that such anomalous behavior in energy storage is attributed to the restricted ion diffusion within the densely packed CNTs in bass carbon channels.

In electric double-layer supercapacitors (EDLCs), two layers of opposite charges are held together by electrostatic forces, forming a Stern layer at the electrode–electrolyte interface.[1–4] This layer significantly contributes to the capacitance as it acts as an effective dielectric separating the electrode from the bulk electrolyte. Porous materials with a high specific surface area provide more sites for Stern layer formation.[5] However, those micropores may have a compact Stern layer, leading to limited ion accessibility, increased steric hindrance, and then reduced ions adsorption, thereby diminishing the contribution of the Stern layer to overall capacitance.[6–8] For example, Hemp-derived activated carbon exhibits reduced capacitance as micropore volume increases, due to limited Stern layer formation. It has been attributed to the coupling effect of ion sizes and pore sizes.[6,7,9,10] In addition to the Stern layer, the capacitance can be affected by the diffuse layer. A wide diffuse layer may lead to low capacitance, whereas a narrow layer can facilitate high capacitance. Such a diffuse width depends on the Debye length as well, which denotes the level of charge screening in the electrolyte. A shorter Debye length will result in a higher ion concentration, a narrower diffuse layer, and then better electrochemical performance.[7,11] In this layer, as the ions are mobile, the diffusion of ions is dictated by boundary conditions. If the channel size is greater than the Debye length, the electric double layer (EDL) forms independently on each wall of channels without significant overlap. The capacitance will primarily depend on the available surface area and ion accessibility. For the channel size is smaller than the Debye length, the diffuse layers from opposing walls overlap each other, leading to that the ions from one wall's EDL are influenced by the electric field of the opposite wall (see Fig. 1). The electrolyte ions in overlapping regions cannot fully screen the surface charges on walls, bringing a weaker charge separation and reduced capacitance.[12–14] For example, the effective electrochemical surface area did not reach the total physical surface area in nanoporous Pt and mesoporous carbon electrode due to EDL overlap.[13] Therefore, the competition between channel sizes and Debye length could significantly affect the electrochemical performance of EDLCs.

To reproduce the scenario of competition between channel size and Debye length, a porous material with controlled channel sizes is needed. For EDLCs, carbon-based materials, such as graphite,[15,16] carbon nanotubes (CNTs),[17–20] and activated carbon,[21,22] have been widely investigated. Among them, CNTs have garnered significant attention as electrode materials for supercapacitors, due to their high surface area and excellent electrical conductivity.[23] The high surface area facilitates the formation of EDL; meanwhile, their conductivity enables faster ion transport. To date, various CNT-based electrodes

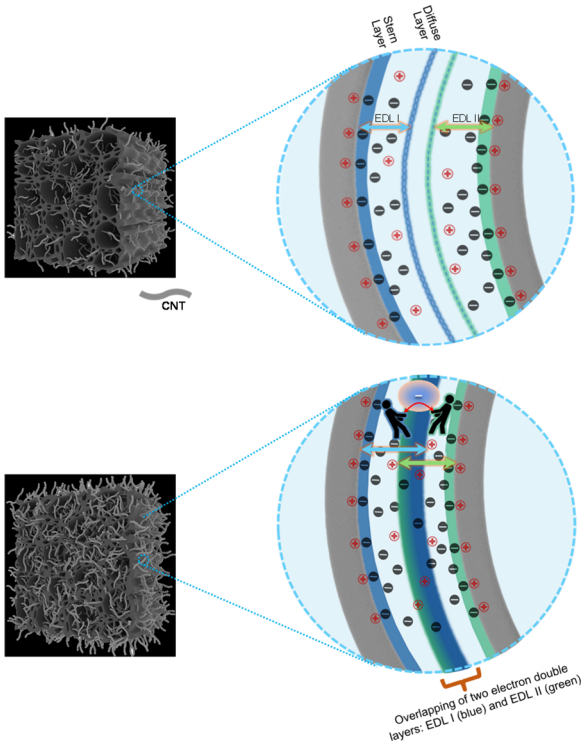

FIG. 1. Schematic illustration of EDL perturbation caused by the narrow spacing between CNTs, leading to overlapping and competition among adjacent EDLs.

have been designed and fabricated to explore their potential toward EDLCs.[17,19] Researchers have also focused on increasing the density of CNTs, aiming to boost the physical surface area.[19,24] For example, vertically aligned CNT forests were synthesized on a graphene substrate to create a three-dimensional (3D) hybrid architecture, exhibiting an exceptionally high specific surface area (SSA) of 2285 $m^2\ g^{-1}$ and outstanding super capacitive performance. Whether the CNT density dictates the supercapacitance is unknown.[24] Notably, CNTs have been grown into biomass carbon channels, offering extensive surface area and enhancing electrochemical performance.[25,26] The well-defined and interconnected pore structure allows for the penetration and diffusion of electrolyte ions into the electrode. The macropores such as channels in biomass carbon hierarchical structures and spacing between CNTs act as reservoirs, reducing resistance and supporting ion mobility.[26,27] Micropores originating from both the biomass-derived carbon and the CNTs contribute substantially to charge storage due to their high specific surface area, while mesopores facilitate ion diffusion, thereby enhancing transport efficiency.[26] However, there is a lack of comparative studies that directly correlate CNT density with electrochemical performance.[25,26] Given the critical role CNTs play in charge storage, the influence of their density on energy storage behavior warrants careful consideration. If CNT density can be precisely controlled within a porous biomass carbon matrix, it would enable a more thorough understanding of how channel size and the Debye length govern energy storage mechanisms.

Herein, we carbonized basswood that was used as skeleton for *in situ* CNT growth. The density of the CNTs varied with the thickness of the bass carbon sheets. Briefly, the small thickness of bass carbon sheet enables full contact of all bass carbon surface with CNT precursors, leading to a denser growth of CNTs. With the electrochemical testing, the density of CNTs can be pinpointed to energy storage capacities, from which the competition between channel size and Debye length can be well understood. For example, the electrochemical impedance spectroscopy (EIS) of the electrode–electrolyte interface is further calculated, and equivalent circuits were assigned to understand the resistance of the system. This work provides an understanding of optimization of the *in situ* growth of CNTs in biomass carbon along with porous electrode materials.

The EDL forms at the interface between an electrode and an electrolyte, consisting of a tightly bound layer of counter-ions near the electrode surface (Stern layer) and a diffuse region where ion concentration gradually returns to bulk values. The organization of ions in this structure is critical for facilitating efficient ion flow and charge storage. Perturbation of the EDL may lead to uneven ion densities or chaotic ion motion, limiting their ability to contribute to charge transfer reactions. Specifically, overlapping electric fields from adjacent or opposing interfaces can distort the regular ion arrangement in the EDL, reducing the field gradient responsible for maintaining ion proximity near the electrode surface. Figure 1 schematically demonstrates such a scenario. As the density of CNTs in carbon channels increases, the spacing among CNTs will significantly decrease. As a result, the diffusion and Stern layer of adjacent CNTs interfere each other. The ion flow through dense CNTs experiences more resistance than passing sparse CNTs in carbon channels. The loss of ideal ion packing within the EDL decreases the total charge density available at the electrode interface, lowering the effective electrochemical capacitance in energy storage. To fully elaborate such an effect, CNTs were grown into the bass carbon channels. Interestingly, the density of CNTs depends on the thickness of bass carbon sheets, which offers opportunity to build up relationships between pore spacing refined by CNTs, Debye length, impedance, and energy storage performance.

For the fabrication of CNTs/bass carbon (CNTs/BC) electrode for supercapacitors, briefly, the basswood was cut into sheets along the longitudinal direction and carbonized at 1000 °C. Before growing CNTs, the sheets were first activated by 3M potassium hydroxide (KOH) and loaded with nickel nitrate [$Ni(NO_3)_2$] nanoparticles. During heat treatment, $Ni(NO_3)_2$ nanoparticles were decomposed into NiO and then reduced into Ni nanoparticles under reduction environment. These nanoparticles acted as nucleation sites for the growth of CNTs. The mixture of xylene and ferrocene as carbon precursors and catalysts, respectively, was introduced into the reaction zone for *in situ* growth of CNTs on and in bass carbon sheets with thickness of 0.5, 0.75, and 1.0 mm. The obtained hybrid carbon specimens were named CNTs/BC-0.5, CNTs/BC-0.75, and CNTs/BC-1.0. The details of experimental fabrication, characterization, and electrochemical testing can be found in the supplementary material.

Figure 2 shows the morphology of the bass carbon without and with the growth of CNTs. Elaborated in Figs. 2(a) and 2(b), the bass carbon is composed of large and small channels with size of ~40 and ~10 μm, respectively. For all three types of bass carbon sheets, the channels pass through the longitudinal direction [see Fig. 2(c)], allowing CNT precursors to nucleate and grow into CNTs. A great number of pores are found in the walls of channels as shown in Fig. 2(d), which may facilitate the flow of precursor molecules during CNT growth and

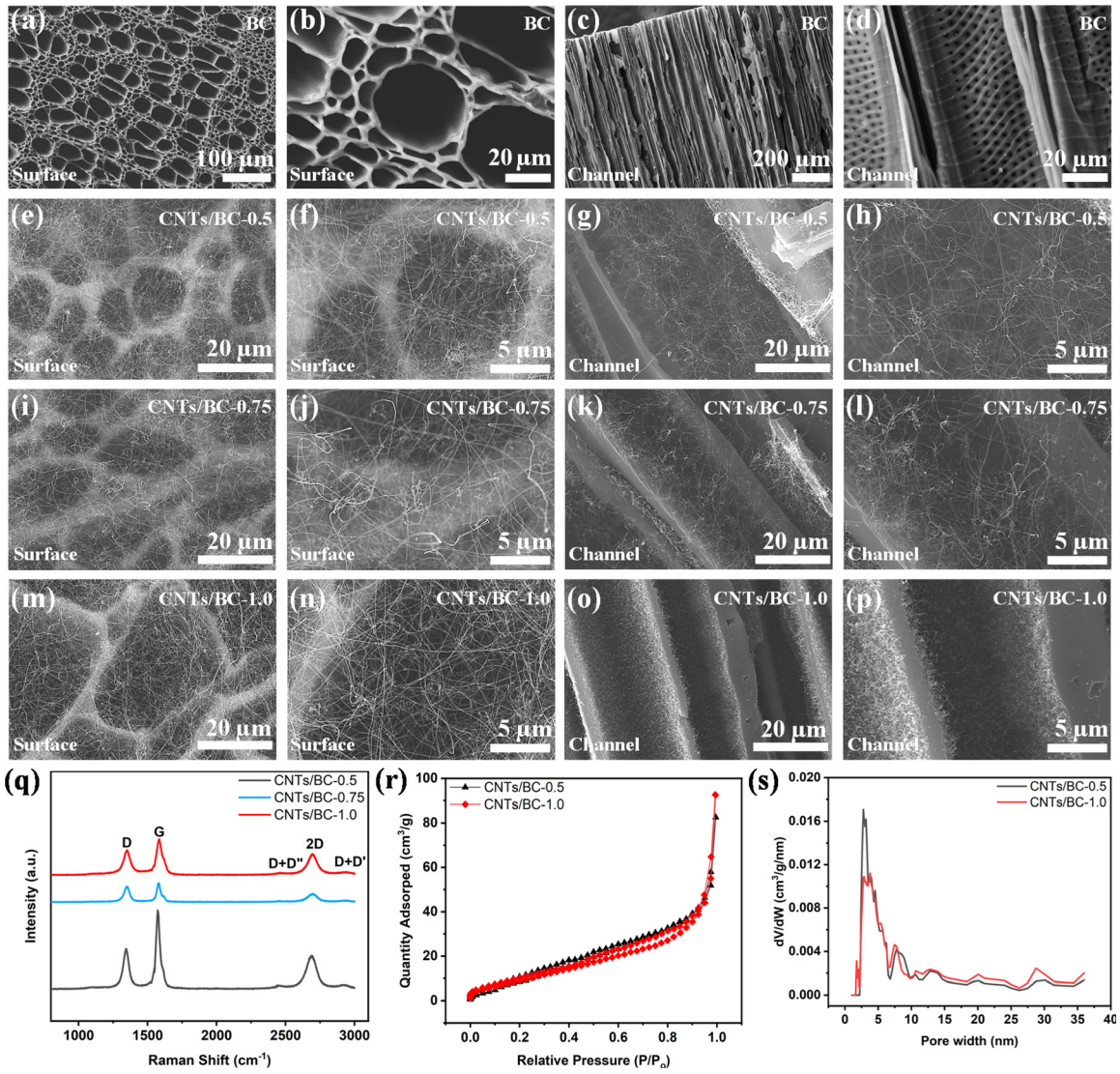

FIG. 2. Morphology and structure of BC without and with the growth of CNTs. SEM images of pristine BC: (a) and (b) surface and (c) and (d) channels. SEM images of CNTs/BC-0.5: (e) and (f) surface and (g) and (h) channels. SEM images of CNTs/BC-0.75: (i) and (j) surface and (k) and (l) channels. SEM images of CNTs/BC-1.0: (m) and (n) surface and (o) and (p) channels. (q) Raman spectra of CNTs/BC with all three thicknesses. (r) N_2 adsorption/desorption isotherms of CNTs/BC-0.5 and CNTs/BC-1.0. (s) Density functional theory (DFT) pore size distributions of CNTs/BC-0.5 and CNTs/BC-1.0.

ion transport during charging and discharging. The bass carbon sheets were precisely milled to thickness of 1.0, 0.75, and 0.5 mm for CNT growth. As evidenced in Figs. 2(e), 2(f), 2(i), 2(j), 2(m), and 2(n), the sheet surface exhibits uniform CNT coverage with comparable densities. Such uniformity is attributed to the even distribution of precursor across the bass carbon sheet, ensuring that all surface receives an equal amount, thereby promoting consistent CNT growth. However, significant variations in the CNT density were observed within the bass carbon channels. In the 0.5 mm thick sheets [CNTs/BC-0.5 shown in Figs. 2(g) and 2(h)], CNTs occupy the entire channel space, with notable entanglement between CNTs grown from opposing channel walls. In contrast, the 1.0 mm thick sheets [CNTs/BC-1.0 shown in Figs. 2(o) and 2(p)] exhibit incomplete channel coverage, with minimal CNT entanglement, as shown in Fig. 2(p). These differences in the CNT density are primarily due to the limited penetration of precursor into deeper regions of thicker samples. This variation offers a means to precisely control CNT density, thereby influencing ion transport and impacting the diffusion resistance in the CNTs/BC.

The morphology analysis of individual CNTs and catalysts in CNTs through a transmission electron microscope (TEM) can be found in the supplementary material Fig. S1. In addition to morphology analysis, the structure and porosity of CNTs/BC were also characterized. Raman spectroscopy was performed on all samples to confirm the growth of CNTs and evaluate their degree of graphitization

[see Fig. 2(q)]. The D peak, located around 1340 cm^{-1}, is associated with defects in sp^2 or sp^3 hybridized carbon, while the G peak at ~1570 cm^{-1} corresponds to the graphitic structure of sp^2 carbon, arising from the in-plane stretching of C-C bond in the graphene.[28–31] The absence of G peak split suggests the predominant formation of multiwalled CNTs.[29,32] Additionally, the peak at ~2690 cm^{-1}, an overtone of the D, is associated with crystallinity of nanotubes.[31] The presence of a distinct 2D peak further confirms the formation of crystalline CNTs. The I_D/I_G ratio of CNTs/BC-0.5 and CNTs/BC-1.0 is higher than that typically seen in CNTs peak due to the presence of amorphous carbon from carbonization of basswood.[29] Notably, the I_D/I_G ratio of CNTs/BC-0.5 is much higher than that for CNTs/BC-1.0 indicating more extensive CNT growth and coverage in the 0.5 mm specimen. This result aligns well with the observation from SEM images.

To investigate and compare the porosity of CNTs/BC with different thicknesses, the Brunauer–Emmett–Teller (BET) surface measurement was conducted. Figures 2(r) and 2(s), respectively, show the N_2 adsorption–desorption isotherms and pore size distributions for samples with thickness of 0.5 and 1.0 mm. Both samples exhibit nearly identical type IV with H4 hysteresis loop, as classified by the IUPAC, indicating the presence of mesoporous structure.[33,34] In both the dominant pore width falls between ~3 and 7 nm, with wide pore distribution spanning to ~40 nm as presented in Fig. 2(s). The slightly higher pore volume around ~3.5 nm in the 0.5 mm sample may result from the denser growth of CNTs on the bass carbon, which could affect the ion transport and conductivity. The calculated specific surface area (SSA) is 47.6 m^2 g^{-1} for the 0.5 mm sample and 39.7 m^2 g^{-1} for the 1.0 mm sample. Despite the significant difference in the CNT density between CNTs/BC-0.5 and CNTs/BC-1.0, the surface areas and pore size distributions are quite similar, which suggests that CNTs/BC-0.75 would have comparable results. The slightly higher SSA in the 0.5 mm sample further supports the presence of a more compact CNTs in the 0.5 mm sample.

To evaluate the impact of CNT density on the energy storage performance, CNTs/BC was used as a free-standing electrode for charging and discharging. The use of free-standing electrodes offers two key advantages: (1) eliminating the need for a current collector, thereby avoiding poor adhesion between active materials and the collector, which can introduce interface resistance; and (2) removing nonconductive binders, preventing additional resistance at the active materials–binder interface.[27,35] Consequently, the electrochemical performance observed is solely based on the intrinsic properties of the CNTs/BC electrode. This study systematically investigated how the *in situ* grown CNT density, both on the surface and within the channels of biomass carbon, impacts the electrochemical behavior of carbon materials, which would help answer if the denser CNTs in channels can always deliver a higher energy storage capacity.

The obtained pristine CNTs/BC sheets were evaluated using a three-electrode system, where the CNTs/BC sheets served as the working electrode, a platinum (Pt) sheet as the counter electrode, and an Ag/AgCl as the reference electrode. Electrochemical testing was performed in 6M KOH electrolyte. The CV measurements were performed for all three CNTs/BC sheets with thicknesses of 0.5, 0.75, and 1.0 mm, within a potential window of 0.1–0.9 V at a scan rate of 1 mV s^{-1}, as shown in Fig. 3(a). Notably, the 1.0 mm sample enclosed the largest area between the charging and discharging curves, while the 0.5 mm sample enclosed the smallest area, despite its highest CNT density. This observation is particularly significant, as a higher CNT density is typically associated with enhanced electrochemical performance. Given the superior performance of the 1.0 mm sample, more detailed electrochemical characterizations including cyclic voltammetry, galvanometric charge–discharge (GCD), and calculated capacitance can be found in supplementary material Fig. S2. Figure 3(b) presents the GCD curves at a current density of 1 mA cm^{-2}. The nearly triangular and symmetrical shape of the curves suggests efficient ion transport during both charging and discharging processes.[27,36] Consistent with the CV results, the GCD analysis confirms the superior electrochemical performance of the 1.0 mm sample. Capacitance calculations at various current densities for all samples [see Figs. 3(c) and 3(d)] further prove this observation. At 1 mA cm^{-2}, the 1.0 mm sample exhibits an aerial capacitance of 6810 mF cm^{-2}, significantly outperforming the 0.5 mm sample, which displays a capacitance of 432 mF cm^{-2}. The 0.75 mm sample demonstrates intermediate performance, aligning with its CNT density. The performance trend persists across increasing current densities. To understand this unique behavior, EIS was conducted for the 0.5 and 1.0 mm samples. The full EIS spectra are shown in Fig. 3(e), with a magnified view of the high-frequency region presented in Fig. 3(f). The EIS spectrum of the 0.5 mm sample exhibits a longer tail in the low-frequency region compared to the 1.0 mm sample, suggesting hindrance of ion diffusion, as low-frequency behavior is associated with diffusion processes.[37–40] However, no significant difference is observed in the high-frequency region. This clearly suggests that the inferior performance of the 0.5 mm sample is primarily attributed to ion diffusion limitations. Moreover, given that the Debye length of the 6M KOH electrolyte is approximately 0.2 nm, it is significantly smaller than the pore size of the electrode as shown in Fig. 2(s). Therefore, the ion transport is predominantly governed by bulk transport behavior, which is mainly affected by the diffusion of the ions.

To better understand the role of ion diffusion in energy storage, the EIS curves for both samples with thicknesses of 0.5 and 1.0 mm were fitted using equivalent circuit elements[38,40] [see Figs. 3(g) and 3(h)]. The details of the equivalent circuit elements can be found in supplementary material Fig. S3. The value of each element is listed in Table I. The equivalent resistance, which represents the electrode–electrolyte interface resistance, is similar for both samples. However, the double-layer capacitance (C_{dl}), corresponding to the EDL formation, is higher in the 0.5 mm sample (0.0082 F) than in the 1.0 mm sample (0.0022 F), which is attributed to the higher CNT density in the thinner electrode. This increase is attributed to the higher CNT density in the thinner electrode, which promotes the initial development of a well-defined Stern layer and facilitates greater EDL formation.

Nevertheless, this denser CNT configuration introduces critical electrochemical limitations. As the spacing between adjacent CNTs decreases, their respective EDLs begin to overlap both physically and electrostatically, causing significant perturbation to the local ionic environment. This overlap leads to electrostatic competition among neighboring EDLs for counter-ions, diminishing the effective surface area for charge storage and ultimately suppressing the individual capacitive contributions of the CNTs. This phenomenon is evidenced by the sharp increase in the charge transfer resistance (R_{ct}) from 0.1628 to 3.227 Ω when transitioning from the 1.0 mm to the denser 0.5 mm CNTs/BC sheet [Figs. 2(g) and 2(h)]. The overlapping EDLs create a zone of electrostatic repulsion that significantly impedes charge transfer across the electrode–electrolyte interface.

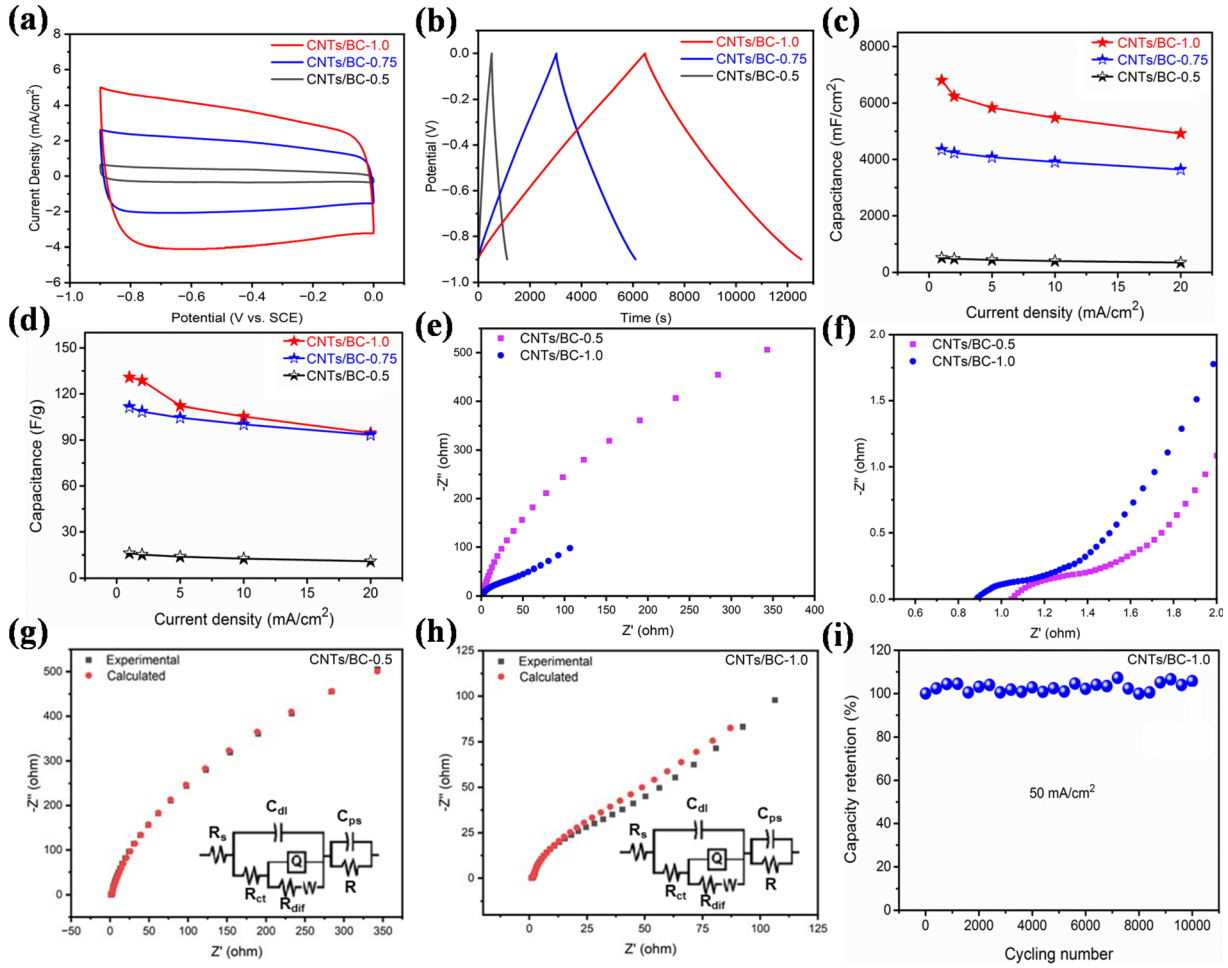

FIG. 3. Electrochemical testing of CNTs/BC. (a) Cyclic voltammetry (CV) curves of CNTs/BC with all three thicknesses measured at a current density of 1 mV/s. (b) Galvanometric charge–discharge (GCD) curves of CNTs/BC with all three thicknesses measured at 1 mA/cm^2. (c) Areal capacitance of CNTs/BC with all three thicknesses calculated at various current densities. (d) Gravimetric capacitance of CNTs/BC with all three thicknesses calculated at various current densities. (e) Nyquist plots for CNTs/BC-0.5 and CNTs/BC-1.0 with frequency ranging from 0.01 Hz to 100 kHz. (f) The Nyquist plots for CNTs/BC-0.5 and CNTs/BC-1.0 under high frequency region. (g) Nyquist plot fitting along with equivalent circuit for CNTs/BC-0.5. (h) Nyquist plot fitting along with equivalent circuit for CNTs/BC-1.0. (i) Cyclic performance of CNTs/BC-1.0 tested at a current density of 50 mA/cm^2 for 10 000 cycles.

TABLE I. Value of each equivalent element obtained from EIS curve fitting.

Equivalent circuit elements	CNTs/BC-0.5	CNTs/BC-1.0
R_s (Ω)	1.1910	1.0560
C_{dl} (F)	0.0082	0.0022
R_{ct} (Ω)	3.2270	0.1628
Q (S.sec$^{\wedge n}$)	0.0072 (n = 0.6916)	0.0386 (n = 0.6452)
R_{dif} (Ω)	446	0.0345
W (S.sec$^{\wedge n}$)	0.000 24	3.23×10^{-9}
C (F)	0.000 75	1.88×10^{-5}
R (Ω)	0.595 30	0.000 19

Furthermore, the narrow interstitial voids between densely packed CNTs restrict electrolyte penetration and hinder ion diffusion, as reflected in the substantial increase in the diffusion resistance (R_{dif}) from 0.0345 Ω in the 1.0 mm sample to 446 Ω in the 0.5 mm sample. These elevated diffusion barriers are the result of intensified electrostatic interactions and physical confinement within the porous CNT network. Such a scenario is schematically illustrated in Fig. 1. The cumulative effect is reduced ion mobility, higher internal resistance, and lower accessible capacitance. This trade-off highlights a fundamental constraint in designing high-density CNT electrodes: while increased surface area and conductivity are theoretically favorable, excessive densification disrupts interfacial charge dynamics and ion transport. Notably, only the 1.0 mm sample exhibits excellent electrochemical stability, retaining nearly constant capacitance over 10 000

charge–discharge cycles [Fig. 3(i)], suggesting that a moderate CNT density better preserves EDL integrity and structural resilience during prolonged operation.

In summary, we designed and fabricated a hybrid biomass-carbon/CNTs electrode material with varying CNT densities. Despite having the highest CNT density, interestingly, the CNTs/BC-0.5 electrode exhibited the poorest electrochemical performance. This counterintuitive observation originates from the following: (1) High charge transfer resistance: As the spacing between adjacent CNTs decreases, their respective EDLs begin to overlap, leading to electrostatic competition among neighboring EDLs for counter-ions, diminishing the effective surface area for charge storage. As a result, the charge transfer resistance increases significantly from 0.1628 Ω in CNTs/BC-1.0 to 3.227 Ω in CNTs/BC-0.5. (2) Elevated diffusion barrier: The narrow interstitial voids between densely packed CNTs restrict electrolyte penetration and hinder ion diffusion, as reflected in the substantial increase in R_{dif} from 0.0345 Ω in the 1.0 mm sample to 446 Ω in the 0.5 mm sample. The elevated diffusion barrier is the result of intensified electrostatic interactions and physical confinement within the porous CNT network. The investigation in this study elaborates how *in situ* grown CNTs in biomass carbon channels affect electrochemical behavior and would guide the design of hybrid electrode materials. The understanding of EDL behavior and ionic transport in nanostructured carbon systems could be continued through integrating materials modeling, electrochemical theory, and advanced characterization techniques.

See the supplementary material for experimental details, TEM imaging, electrochemical testing, and EIS analysis.

We acknowledge the funding support from the USDA Forest Service through Grant Nos. 23-JV-11111124-016 and 24-JV-11111124-100. Special thanks are also given to Timothy Ketelboeter, and Joseph Destree at USDA Forest Products Laboratory, for their help in making this project run successfully.

AUTHOR DECLARATIONS

Conflict of Interest

The authors have no conflicts to disclose.

Author Contributions

Manish Neupane: Conceptualization (equal); Data curation (lead); Formal analysis (lead); Writing – original draft (lead); Writing – review & editing (equal). **Xiahua Zhong:** Formal analysis (equal); Writing – review & editing (equal). **Guanhui Gao:** Data curation (equal); Formal analysis (equal); Writing – review & editing (equal). **Qiangu Yan:** Formal analysis (equal); Writing – review & editing (equal). **Jinwu Wang:** Writing – review & editing (equal). **Zhiyong Cai:** Funding acquisition (lead); Writing – review & editing (equal). **Yingchao Yang:** Conceptualization (equal); Formal analysis (equal); Funding acquisition (equal); Resources (equal); Supervision (equal); Writing – original draft (equal); Writing – review & editing (equal).

DATA AVAILABILITY

The data that support the findings of this study are available from the corresponding authors upon reasonable request.

REFERENCES

[1]J. Q. Shang, K. Y. Lo, and R. M. Quigley, Can. Geotech. J. **31**(5), 624–636 (1994).
[2]D. Henderson and D. Boda, Phys. Chem. Chem. Phys. **11**(20), 3822–3830 (2009).
[3]H. Helmholtz, Ann. Phys. **165**(6), 211–233 (1853).
[4]D. G. Grahame, Chem. Rev. **41**(3), 441–501 (1947).
[5]G. Salitra, A. Soffer, L. Eliad, Y. Cohen, and D. Aubach, J. Electrochem. Soc. **147**(7), 2486 (2000).
[6]H. Wang and L. Pilon, J. Phys. Chem. C **115**(33), 16711–16719 (2011).
[7]J. Huang, B. G. Sumpter, and V. Meunier, Angew. Chem., Int. Ed. **47**(3), 520–524 (2008).
[8]K. Murota and T. Saito, Phys. Chem. Chem. Phys. **24**(30), 18073–18082 (2022).
[9]W. Sun, S. M. Lipka, C. Swartz, D. Williams, and F. Yang, Carbon **103**, 181–192 (2016).
[10]J. Huang, R. Qiao, B. G. Sumpter, and V. Meunier, J. Mater. Res. **25**(8), 1469–1475 (2010).
[11]C. Ma, Y. Yu, Y. Li, J. Shi, Y. Song, and L. Liu, J. Electrochem. Soc. **161**(9), A1330–A1337 (2014).
[12]P. Wu, J. Huang, V. Meunier, B. G. Sumpter, and R. Qiao, ACS Nano **5**(11), 9044–9051 (2011).
[13]H. C. Lee, J. Kim, H. J. Yang, J. Yu, and J. H. Bae, Anal. Chem. **96**(47), 18745–18753 (2024).
[14]S. Das and S. Chakraborty, Phys. Rev. E **84**(1), 012501 (2011).
[15]S. R. Sivakkumar, J. Y. Nerkar, and A. G. Pandolfo, Electrochim. Acta **55**(9), 3330–3335 (2010).
[16]H. K. Jeong, M. Jin, E. J. Ra, K. Y. Sheem, G. H. Han, S. Arepalli, and Y. H. Lee, ACS Nano **4**(2), 1162–1166 (2010).
[17]M. Noked, S. Okashy, T. Zimrin, and D. Aurbach, Angew. Chem., Int. Ed. **51**(7), 1568–1571 (2012).
[18]J. Benson, I. Kovalenko, S. Boukhalfa, D. Lashmore, M. Sanghadasa, and G. Yushin, Adv. Mater. **25**(45), 6625–6632 (2013).
[19]D. N. Futaba, K. Hata, T. Yamada, T. Hiraoka, Y. Hayamizu, Y. Kakudate, O. Tanaike, H. Hatori, M. Yumura, and S. Iijima, Nat. Mater. **5**(12), 987–994 (2006).
[20]E. Frackowiak, K. Metenier, V. Bertagna, and F. Beguin, Appl. Phys. Lett. **77**(15), 2421–2423 (2000).
[21]M. Vijayakumar, R. Santhosh, J. Adduru, T. N. Rao, and M. Karthik, Carbon **140**, 465–476 (2018).
[22]V. Barranco, M. A. Lillo-Rodenas, A. Linares-Solano, A. Oya, F. Pico, J. Ibañez, F. Agullo-Rueda, J. M. Amarilla, and J. M. Rojo, J. Phys. Chem. C **114**(22), 10302–10307 (2010).
[23]C. G. Liu, M. Liu, F. Li, and H. M. Cheng, Appl. Phys. Lett. **92**(14), 143108 (2008).
[24]Y. Zhu, L. Li, C. Zhang, G. Casillas, Z. Sun, Z. Yan, G. Ruan, Z. Peng, A. O. Raji, C. Kittrell, R. H. Hauge, and J. M. Tour, Nat. Commun. **3**(1), 1225 (2012).
[25]C. Wu, S. Zhang, W. Wu, Z. Xi, C. Zhou, X. Wang, Y. Deng, Y. Bai, G. Liu, X. Zhang, X. Li, Y. Luo, and D. Chen, Carbon **150**, 311–318 (2019).
[26]Q. He, R. He, A. Zia, G. Gao, Y. Liu, M. Neupane, M. Wang, Z. Benedict, K. K. Al-Quraishi, L. Li, P. Dong, and Y. Yang, Small **18**(50), 2200272 (2022).
[27]M. Neupane, Q. Yan, R. He, R. Masmoudi, Y. Liu, Z. Benedict, J. Wang, C. Tripp, P. Dong, Z. Cai, and Y. Yang, Batteries Supercaps **6**(9), e202300193 (2023).
[28]J. Xiao, B. Wen, X. Liu, Y. Chen, J. Niu, S. Yang, W. Yuan, M. Yu, G. Yang, and S. Ding, J. Colloid. Interface Sci. **676**, 33–44 (2024).
[29]Z. Li, L. Deng, I. A. Kinloch, and R. J. Young, Prog. Mater. Sci. **135**, 101089 (2023).
[30]A. C. Ferrari, Solid State Commun. **143**(1–2), 47–57 (2007).
[31]E. F. Antunes, A. O. Lobo, E. J. Corat, and V. J. Trava-Airoldi, Carbon **45**(5), 913–921 (2007).
[32]S. Piscanec, M. Lazzeri, J. Robertson, A. C. Ferrari, and F. Mauri, Phys. Rev. B **75**(3), 035427 (2007).
[33]H. Li, Y. Gong, C. Fu, H. Zhou, W. Yang, M. Guo, M. Li, and Y. Kuang, J. Mater. Chem. A **5**(8), 3875–3887 (2017).
[34]M. D. Donohue and G. L. Aranovich, J. Colloid Interface Sci. **205**(1), 121–130 (1998).

[35]H. P. Cong, X. C. Ren, P. Wang, and S. H. Yu, Energy Environ. Sci. **6**(4), 1185–1191 (2013).
[36]R. He, M. Neupane, A. Zia, X. Huang, C. Bowers, M. Wang, J. Lu, Y. Yang, and P. Dong, Adv. Funct. Mater. **32**(49), 2208040 (2022).
[37]A. C. Lazanas and M. I. Prodromidis, ACS Meas. Sci. Au **3**(3), 162–193 (2023).
[38]N. Meddings, M. Heinrich, F. Overney, J. S. Lee, V. Ruiz, E. Napolitano, S. Seitz, G. Hinds, R. Raccichini, M. Gaberšček, and J. Park, J. Power Sources **480**, 228742 (2020).
[39]B. A. Mei, O. Munteshari, J. Lau, B. Dunn, and L. Pilon, J. Phys. Chem. C **122**(1), 194–206 (2018).
[40]M. Arunkumar and A. Paul, ACS Omega **2**(11), 8039–8050 (2017).